Ocean Dynamics (2012) 62:725–740
DOI 10.1007/s10236-012-0521-0

A short-term predictive system for surface currents from a rapidly deployed coastal HF radar network

Donald Barrick · Vicente Fernandez · Maria I. Ferrer · Chad Whelan · Øyvind Breivik

Received: 12 September 2011 / Accepted: 3 January 2012 / Published online: 22 January 2012

Abstract In order to address the need for surface trajectory forecasts following deployment of coastal HF radar systems during emergency-response situations (e.g., search and rescue, oil spill), a short-term predictive system (STPS) based on only a few hours data background is presented. First, open-modal analysis (OMA) coefficients are fitted to 1-D surface currents from all available radar stations at each time interval. OMA has the effect of applying a spatial low-pass filter to the data, fills gaps, and can extend coverage to areas where radial vectors are available from a single radar only. Then, a set of temporal modes is fitted to the time series of OMA coefficients, typically over a short 12-h trailing period. These modes include tidal and inertial harmonics, as well as constant and linear trends. This temporal model is the STPS basis for producing up to a 12-h current vector forecast from which a trajectory forecast can be derived. We show results of this method applied to data gathered during the September 2010 rapid-response demonstration in northern Norway. Forecasted coefficients, currents, and trajectories are compared with the same measured quantities, and statistics of skill are assessed employing 16 24-h data sets. Forecasted and measured kinetic variances of the OMA coefficients typically agreed to within 10–15%. In one case where errors were larger, strong wind changes are suspected and examined as the cause. Sudden wind variability is not included properly within the STPS attack we presently employ and will be a subject for future improvement.

Keywords HF radar · Ocean forecasting · Search and rescue · Oil spill

Responsible Editor: Michel Olagnon

This article is part of the Topical Collection on *Advances in Search and Rescue at Sea*

D. Barrick · C. Whelan (✉)
CODAR Ocean Sensors,
1914 Plymouth Street,
Mountain View, CA, USA
e-mail: chad@codar.com

V. Fernandez · M. I. Ferrer
Qualitas Remos,
C/Toronga, 31,
Madrid, Spain

Ø. Breivik
The Norwegian Meteorological Institute,
Bergen, Norway

Ø. Breivik
Geophysical Institute, University of Bergen,
Bergen, Norway

1 Introduction

HF coastal radars have evolved over the past 40 years into worldwide operational networks that provide real-time data to a variety of end users. Over 450 such radars are operating today, of which about 400 are CODAR SeaSondes®. The primary data products are 2-D surface current vector maps, which require two or more radars with overlapping coverage (Barrick et al. 1977; Lipa and Barrick 1983). In addition to surface currents, secondary outputs include wave parameters (Lipa and Barrick 1986), tsunami detections (Barrick 1979; Lipa et al. 2011), and vessel detections (Roarty et al. 2011). The fate of anything floating on the surface, such as vessels adrift or oil/pollutant spills, are highly, if not completely, dependent on surface currents. While the ability of HF radar to provide surface current maps in near real time is of great value, the ability to forecast the currents and, thus, the fate of material floating on the surface is an even more important tool.

Efforts to assimilate HF radar-derived currents into coastal ocean models (Breivik and Sætra 2001; Oke et al. 2002; Paduan and Shulman 2004) that can provide forecasts have been successful, but at the current state, full assimilation of surface current maps into hydrodynamic models can be a laborious process that requires archives and other sources of data. Efforts have also been made to use longer time series of surface current maps to make short-term forecasts (Zelenke 2005; Frolov et al. 2011). As these efforts to produce surface current model forecasts progressed, the U.S. East Coast became populated with a contiguous HF radar ocean monitoring network and the U.S. Coast Guard (USCG) began a program to evaluate SeaSonde data products for use in search and rescue (SAR) operations. Comparisons were performed over many years with self-locating datum marker buoys (Ullman et al. 2003; O'Donnell et al. 2005; Ullman et al. 2006). These evaluations have established conclusively that, in all cases, incorporating radar-derived current fields into short-term predictive systems (STPS) significantly improves SAR capability, efficacy, and reduces costs of search operations. The STPS methods employed in the USCG SAR operations are Monte Carlo random-walk or random-flight models to forecast the advected drift areas. After nearly a decade of such careful test and evaluation, these methods were incorporated into the U.S. Coast Guard operations first beginning 2 years ago for the region from Massachusetts to North Carolina's Cape Hatteras with HF radar surface current data supplied by regions the Mid-Atlantic Regional Association Coastal Ocean Observing System (http//www.maracoos.org). The West Coast is being brought online for SAR operations, from the Mexican border nearly to Canada. Presently, with sparse radar measurements in Gulf of Mexico, southeastern USA, Alaska, Hawaii, and the Caribbean, HF radar in these regions is not included in Coast Guard plans for SAR operations.

A similar emergency application with a need for STPS forecasts is oil spill response. SeaSondes have recently been in place and operating for two separate incidents involving spilled oil. At the time of the 2010 Deepwater Horizon incident in the Gulf of Mexico, during which oil spilled continuously for 5 months, as well as during the 2007 Cosco Busan tanker incident in California's San Francisco Bay, SeaSondes measured surface currents in the affected areas in near real time. These fortuitous measurements proved highly useful to NOAA and other groups managing cleanup operations. In fact, four decades ago, it was the motivation of oil spill environmental assessment that led to funding at NOAA under which HF radar/CODAR was developed into a useful current-mapping tool in the early 1970s.

Norway has evolved an active offshore oil/gas production industry in their sector of the North Sea and has been a leader in application of the latest and best technologies to manage the inevitable spills that accompany such operations. Although a small network of SeaSondes operate near Fedje, the gateway to the Mongstad refinery, nearly the entire Norwegian coast has no radar coverage and is mostly inaccessible by road and land vehicles. In 2010, with funding from the Norwegian Clean Seas Association for Operating Companies (NOFO; http://www.nofo.no) and Innovation Norway, a rapid-response capability was developed in which a SeaSonde pair could be deployed and provide surface currents within hours of a spill (Kjelaas et al. 2011). This culminated in a month-long exercise in Finnmark during September 2010. Figure 1 shows photos of this deployment. The Rapidly Deployable SeaSonde operated in the 13-MHz band, which provided a useful range of about 80 km at 2-km range resolution. Temporal resolution for the averaged cross spectra and, therefore, unaveraged radial vector output was 10 min, and the averaged radial vector output interval was 60 min. The Finnmark exercise demonstrated that such an approach could provide maps of offshore surface currents quickly during an emergency, thereby offering improved information for cleanup operations.

Whereas the USCG and other forecast methods using SeaSonde data employed methodologies that relied on a month or more of historic data to forecast tides and background, this will not be possible in a rapid deployment to a new area. The challenge, therefore, is to draw upon data collected during the first few hours after radar startup to initialize the STPS forecast method. For example, after 8–12 h, enough data should be available to capture the semidiurnal and inertial harmonics, as well as a constant and perhaps linear trend. One might not expect this to be adequate for predictions extending more than an equivalent period into the future.

Fig. 1 Photos of self-contained SeaSonde HF radar being helicopter-deployed in Finnmark region of northern Norway during September 2010, during NOFO emergency-response exercise. Radar antenna is mounted alongside the weatherproof container and portable generator powers the system for up to a week

However, this is considered highly useful in directing operations, either for SAR or spill mitigation.

It is the purpose of this paper to investigate the utility and accuracy of this concept by selecting 16 24-h periods during the NOFO deployment beginning September 14, 2010, 21:00 UTC through September 30, 2010, 22:00 UTC in order to assess the forecast skill of our STPS method. The first 12 h of each period is used as the history/background. The STPS then forecasts currents and derived trajectories ahead for the next 12 h. The latter are then compared with actual observations over the second 12 h and statistics of differences calculated to reveal accuracy. In our first attempts here, wind effects are included only to lowest order. A constant wind as well as a linear variation over the 12-h period is in fact included in our STPS model. However, any shorter-period change—perhaps due to a frontal passage—is not. Expected effects of short-period wind changes are discussed, and a method suggested for dealing with this is proposed.

Section 2 describes the open-mode analysis (OMA) spatial fitting that is applied to the data every hour to obtain modal coefficients that vary with time. Section 3 derives our STPS temporal modal methodology that is applied to the OMA time-varying coefficients. Following this, Section 4 analyzes the forecasted OMA coefficients, current patterns, error statistics, and trajectories with actual measured values based on radar observations with estimations of trajectory displacement differences as a function of time into the future. A case study of short-period wind changes is discussed, and a method suggested for dealing with this is proposed in Section 5. Finally, a discussion of results is provided in Section 6 including additional studies and the possibility of improving predictions by including forecasted winds.

2 Open-mode analysis principles and fitting to NOFO currents

OMA as advanced by Lekien and Coulliette (2004) is an outgrowth of normal mode analysis (NMA), first introduced for SeaSonde HF radar measurements by Lipphardt et al. (2000). Both are based on representing flow near the surface in terms of a divergence-free stream function and vorticity-free velocity potential. Both the stream function and velocity potential are scalar fields depending on x, y that are defined within a horizontal domain that roughly describes the radar coverage area:

(a) Stream function: This scalar field satisfies the following Laplace second-order partial differential equation (PDE):

$$\nabla^2\psi(x,y) = 0 \tag{1}$$

where the Dirichlet condition applies to the boundary, i.e., ψ_Ω=0 where Ω denotes the boundary of the region to be fitted.

(b) Velocity potential: This scalar field satisfies the following Laplace second-order PDE:

$$\nabla^2\phi(x,y) = 0 \tag{2}$$

where the Neumann condition applies to the boundary, i.e., $\hat{n}\cdot\nabla\phi_\Omega = 0$ where $\hat{n}$ denotes the unit vector normal to the boundary Ω.

(c) Boundary function: The main departure of OMA by Lekien and Coulliette (2004) from NMA of Lipphardt et al. (2000) has to do with how the open boundary region is treated. A portion of the boundary is "closed," comprised of relevant coastlines where the Dirichlet and Neumann conditions apply. The remainder is an open boundary where neither of the above conditions can be expected to apply. NMA suggested two somewhat arbitrary ways to deal with the open boundary (including use of data from a model, which may not always be available). In OMA, a third function, and resulting set of modes, was demonstrated that defined a new functional "boundary" field

$$\nabla^2\phi^b(x,y) = 0 \tag{3}$$

that is to be specified on the open boundary in place of the Neumann condition, i.e., by $\hat{n}\cdot\nabla\phi_\Omega = g_\phi(s) \equiv \hat{n}\cdot\overline{u}_{\Omega_0}$, where Ω_0 is the open portion of the boundary Ω and s denotes arc-length distance along the boundary.

(d) Eigenfunction solutions for the three Laplace Eqs. 1, 2, and 3:

$$\nabla^2\psi_i + \lambda_i^\psi\psi_i = 0; \qquad \nabla^2\phi_i + \lambda_i^\phi\phi_i = 0; \qquad \nabla^2\phi_i^b + \lambda_i^b\phi_i^b = 0 \tag{4}$$

Here, the subscripted quantities define eigenfunctions, which we call OMA modes. These modes are functions of x, y; they need to be calculated only once using finite element methods for a given radar geometry and then stored for subsequent use. The subscripted parameters λ_i are the eigenvalues corresponding to that respective set of modes; the latter are always positive, usually arranged in ascending order. The lowest-order modes have the largest spatial extent, fitting to the interior of the boundary domain, with the higher modes capturing the finer spatial details of the current variations.

(e) Surface current expansions in terms of eigen modes: Understanding that x, y are the Cartesian coordinates within the locally planar ocean surface—generally representing east and north, respectively—the expression for the surface current vector along these directions in terms of stream function and velocity potential is:

$$\overline{u}(x,y) = \nabla\times(\psi(x,y)\hat{z}) + \nabla\phi(x,y) + \nabla\phi^b(x,y) \tag{5}$$

This can now be written in terms of our eigenfunction modal expansion as:

$$\overline{u}(x,y,t) = \sum_{i=1}^{\infty} \alpha_i^{\psi}(t_j)\nabla \times \psi_i(x,y)\widehat{z} + \sum_{i=1}^{\infty} \alpha_i^{\phi}(t_j)\nabla\phi_i(x,y) + \sum_{i=1}^{\infty} \alpha_i^{b}(t_j)\nabla\phi_i^{b}(x,y) \quad (6)$$

where we now include time of the measurement (e.g., hourly) as t_j. Thus, every time interval we understand that a new set of OMA coefficients, α_i, are to be fitted (in a linear least-squares (LS) sense) to the radar-observed current fields. It is these sequential time-dependent mode coefficients that are to be used in the STPS method we develop next (rigorous justification for the OMA mathematics summarized above is found in Lipphardt et al. (2000) and Lekien and Coulliette (2004)) These modes can either be fitted to the 2D vectors where measurements of two or more radars overlap and combined prior to modal analysis or they can be fitted to the 1-D measurements (radial velocities) of individual radar sites in their inherent polar coordinate systems (Kaplan and Lekien 2007). We have chosen to fit to the 1-D radial velocities in our investigation, as it has been found to be more robust. The three sets of coefficients in the triple summations above are often referred to as Dirichlet, Neumann, and boundary modes, respectively. Kaplan and Lekien (2007) also show how to calculate errors in the OMA-fitted currents based on errors estimated in the original radial velocities.

(f) Number of modes to use: In the above modal expansions, we show an infinite number of terms/modes in the series. In practice, we must terminate each of these series at some upper limit (not necessarily the same for each set of modes). Although one is often tempted to include all consecutive terms in ascending order of their eigenvalues (which are indexed by subscript *i*), this is not necessarily the best criterion of selecting which modes to retain. A more robust measure may be the kinetic energy contained in the velocities for each fitted mode for the area of interest, in this case the NOFO coverage region; we examine this further below. Other measures have been studied, such as the scale size of the mode area (Lekien and Gildor 2009), which has led to suggestions of hundreds of modes and series terms. We are somewhat wary of this approach because higher-order terms respond to noise, outliers, and gaps in the data, which the OMA concept is meant to filter out. Lekien and Gildor (2009) found, for example, that although many hundred modes appear useful for overall OMA-fitted current maps, divergence and vorticity derived therefrom were unacceptably unstable and noisy when the total mode number exceeded 20 or so; this is a subject that needs further investigation. Experience to date suggests that fewer modes rather than too many may be preferred.

2.1 NOFO case study of OMA domain

The study area (Finnmark, northern Norway) where we have tested the STPS methodology presented in this paper is shown in Fig. 2. For this area, we have defined a fixed domain where modes are computed, shown in Fig. 2, illustrating the open and closed boundaries. Note that the coastline is a natural closed boundary (no normal flow through the shoreline), and we allow flow through the straits between the islands.

2.2 Dominant modes fitted to NOFO OMA domain

In deciding the construction and the number of modes to be used in the OMA fit to the HF data, one limiting factor is the spatial scale that is to be resolved, which should be the same or more coarse resolution than the measurement grid (Lekien and Gildor 2009). In this case, our Cartesian measurement grid spacing was 3 km. Ocean features of 15 km are well resolved

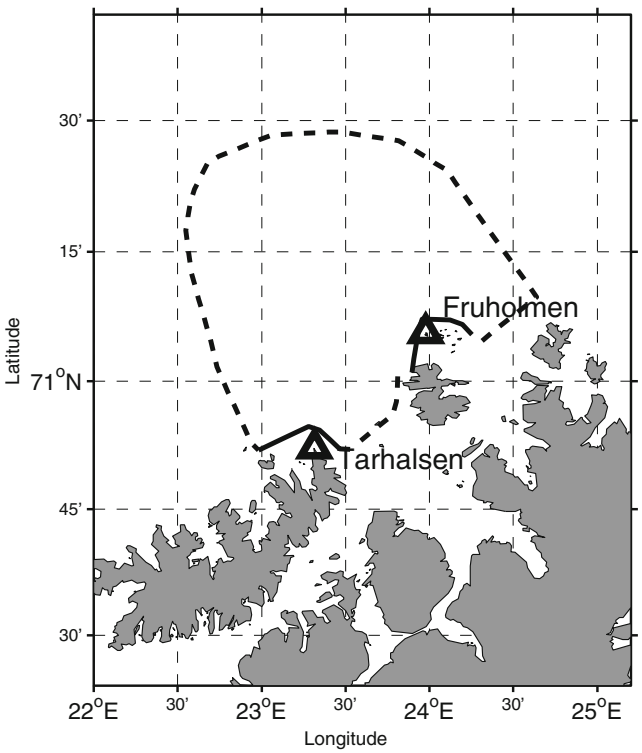

Fig. 2 Domain where the current modes are computed and the surface currents are obtained during the period of the study. The *dashed line* represents the open boundary and the *continuous lines* are the closed lines. The *triangles* represent the two SeaSonde Stations. Tarhalsen station is the mobile unit shown in Fig. 1 and Fruholmen is a fixed station

with the actual horizontal measurement grid resolution of 3 km for the total currents and with the goal in this study of reproducing the modes with the most inertia the choice was made to analyze modes with spatial scales 15 km or larger. With this configuration, we arrive at a total of 34 modes (7 free-divergence, 15 irrotational modes, and 12 boundary modes). In Fig. 3, the two most energetic modes for each type derived from the fit to the radial data are illustrated (see Section 4.1 for a detailed examination of an energy analysis of the modes).

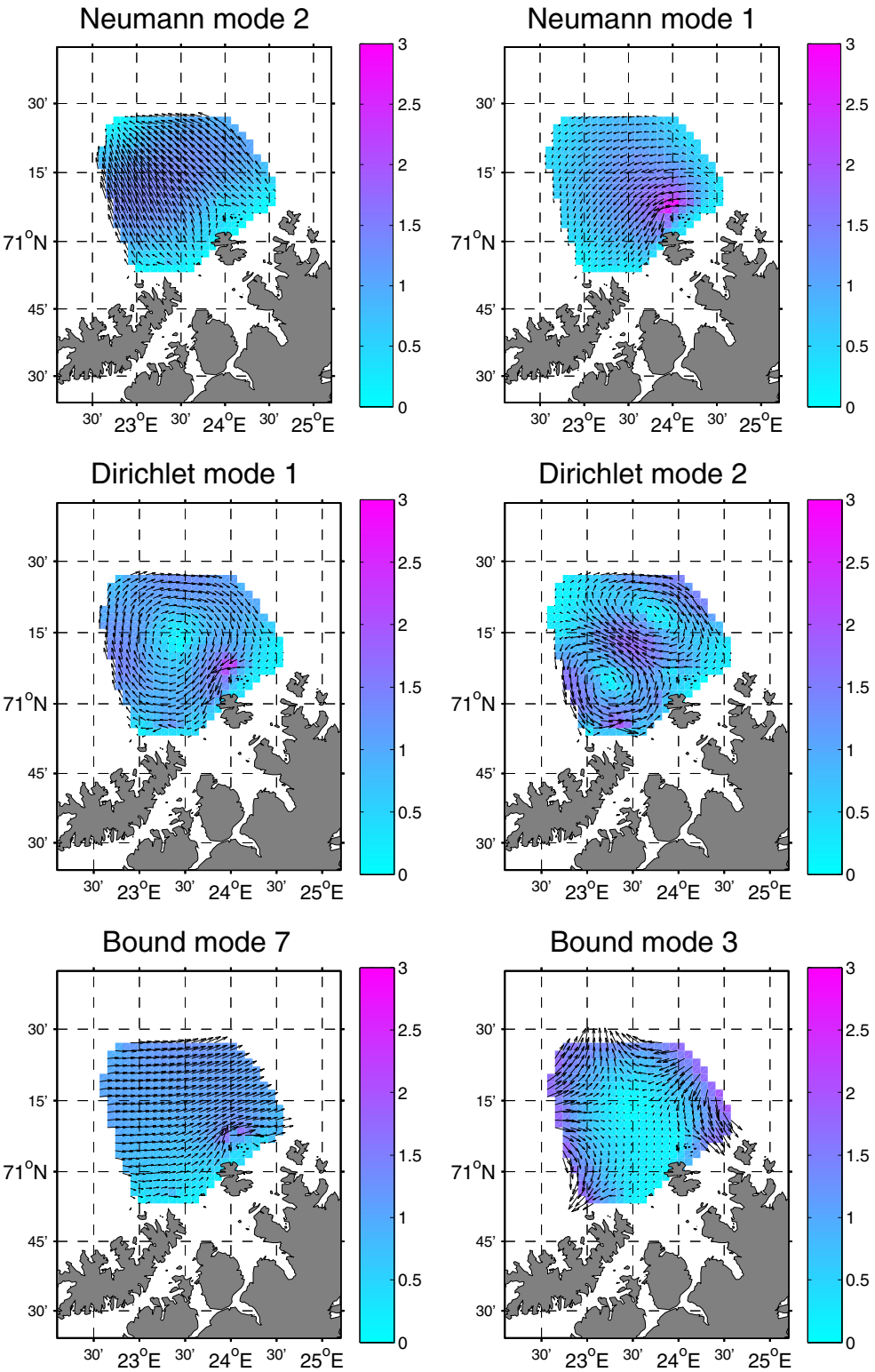

Fig. 3 The two most energetic currents modes for each type (see Section 4.1 for a detailed analysis of the energy of the modes). The *first row* shows the incompressible modes, the *second row* shows the irrotational modes, and the *last row* contains the boundary modes. The *colorbar* is the magnitude of the velocity in centimeters per second

During the duration of the field experiment, the radial data output every hour from the mobile unit at Tarhalsen and from the fixed station at Fruholmen were fitted to an optimal combination of the 34 spatial modes that give a better estimation of the surface current nowcast in the predefined domain. The OMA nowcast fields have the advantage of being free of spatial gaps and with currents only tangent to the coast.

In this fitting process, Kaplan and Lekien (2007) introduce and demonstrate in their Section 3.2 a "homogenization smoothing term," defined by the parameter k, that enters the least-squares cost function; this serves to constrain the fitting so that mode amplitudes that would produce unacceptably large velocities are not allowed. They demonstrate that values for this parameter of 10^{-2} and lower appear optimal, in the sense that they better fit the actual total vector field before application of OMA. We tried both 10^{-1} and 10^{-2} for this parameter and found that indeed, 10^{-2}, produced closer fits to the conventional total vectors in terms of least RMS differences and so have used this value throughout our analysis.

It is instructive to compare graphically the OMA nowcast fields versus total surface vectors obtained by the conventional LS local interpolation method (Lipa and Barrick 1983). This conventional approach draws a circle of user-selected radius around each Cartesian point on the current map grid. It collects all radial velocity vectors from both sites that fall within this circle. Then, it does a straightforward, over-determined least-squares fit of these radials to estimate the *u*/*v* components of the total vector for that grid point. Being a local combining method, the LS method detailed in Lipa and Barrick 1983 is not gap-free and has no kinematic constraints to prevent normal flow through the shoreline. Figure 4 shows the RMS differences between the two methods (OMA-radial-fitted vs. LS) for both components *U* and *V* and show how the differences are smaller in the middle of the domain where the radials give in areas where two radials give more independent information.

Figure 4 was based on an analysis of all 16 periods covering the NOFO data set, each comprising 24 h of data. The overall RMS difference summaries for these figures are 8.6 and 7.8 cm/s for *U* and *V*, respectively. Although we do not show a similar figure for the constraint parameter k=0.1 (the above figure used k=0.01), the corresponding RMS difference summaries for that case were 13.2 and 9.5 cm/s for *U* and *V*, respectively. The lower RMS values justified our selection for k=0.01 for our analyses.

3 STPS modal methodology applied to OMA modes for NOFO

We present and analyze a methodology to operate on a very short time history of measured, OMA-fitted surface current coefficients. We note that success was obtained by Zelenke (2005) to predict up to 48 h in the future, by fitting to annual, seasonal, tidal, and wind forcing components using time series analysis over multiple years of continuous data. In case of an emergency, however, where a SeaSonde is set up at a location without access to a detailed history of tidal and other current climatology, it is desired to have a method to begin providing short-term forecasts after a few hours of data have been collected. We restrict expectation of good forecast accuracy to approximately the same span in the future as the length of the past period on which the forecast is to be based. In particular, because most locations are dominated by semidiurnal, diurnal, and inertial harmonics, as well as constant and linear trend, a ~12-h history set followed by a 12-h forecast seemed like a reasonable goal to seek in our first analyses here. Forecasts farther into the future are possible, perhaps, but certain assumptions and approximations as described in our method below, particularly in relation to the linear trend and simple treatment of tides, will clearly require a different analysis. Additionally, the occurrence of multiple wind or other episodic events becomes much more likely. We are essentially doing a temporal modal expansion of the data set history, in contrast with the OMA spatial modal representation we described above. We selected 16 24-h periods from the NOFO surface currents as a test/evaluation basis.

One might ask why develop a STPS methodology based on OMA-based coefficients over time rather than on some other representation of the surface currents? The OMA

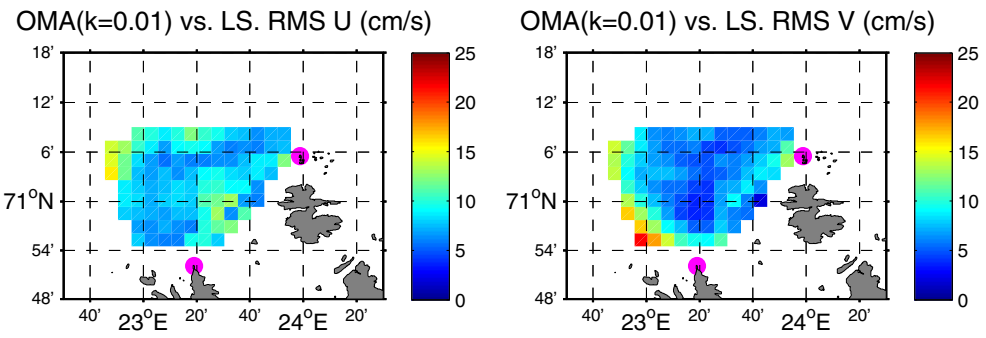

Fig. 4 Root mean square (*RMS*) of the differences in centimeters per second between the OMA-radial-fitted vector fields and the LS method for all of the aforementioned 16 24-h periods. The *U* and the *V* components of the velocity are shown separately

modes, especially the lower-order most energetic ones, represent larger areas with greater kinetic energy. Therefore, they should have some reasonable degree of inertia, i.e., they are more noise free over short periods of time such as an hour or 2. Higher OMA modes representing shorter spatial scales might be expected to exhibit short-term noise that would not follow the slowly varying temporal modes we discussed above. This is also another reason to restrict the number of modes: so that finer-scale spatial variability is not propagated through to the higher-order modes:

(a) OMA coefficient vector: Assume OMA-fitted coefficients have been determined as outlined in the section above, for a short time period for 8–12 h. We can append all three sets of mode coefficients (Neumann, Dirichlet, and boundary) to obtain a single coefficient vector, leaving off the superscript notation. These are:

$$\left[A^{(i)}\left(t_j\right)\right] = \left[A_j^{(i)}\right] \tag{7}$$

where we used $A_j^{(i)}$ to represent $\left[\alpha_i^{\phi}\left(t_j\right);\ \alpha_i^{\psi}\left(t_j\right);\ \alpha_i^{b}\left(t_j\right)\right]$ from the previous section.

(b) The STPS modal temporal representation: For each OMA coefficient designated with superscript *i*, start with a model containing a constant, linear trend, semidiurnal (f_2 for M2) and diurnal (f_1 for K1) tidal constituents, as well as an inertial harmonic $f_o = 2\Omega\sin(\vartheta)$, where f_o is the inertial frequency (all frequencies are understood to be radians/second). Here, ϑ is the latitude of the radar area, and Ω is the earth angular rotation rate in radians/second. In this case, we used the latitude at the midpoint between northernmost and southernmost edges of the OMA domain.

Then we can write the eight-term temporal model we propose as follows:

$$\begin{aligned} A_j^{(i)} &= B_1^{(i)} + B_2^{(i)} t_j + B_3^{(i)}\cos\left(f_1 t_j\right) + B_4^{(i)}\sin\left(f_1 t_j\right) + \\ &+ B_5^{(i)}\cos\left(f_2 t_j\right) + B_6^{(i)}\sin\left(f_2 t_j\right) + B_7^{(i)}\cos\left(f_o t_j\right) + B_8^{(i)}\sin\left(f_o t_j\right) \end{aligned} \tag{8}$$

The temporal modal coefficients $B_n^{(i)}$ are considered to be unknown for each of the *i* OMA modes. These relations can be expressed more compactly in matrix form as:

$$\overbrace{\left[A_j^{(i)}\right]}^{J\times 1} = \overbrace{\left[M_{j,n}\right]}^{J\times N}\overbrace{\left[B_n^{(i)}\right]}^{N\times 1} \tag{9}$$

where the dimensions of the respective matrices are given above the upper brackets. As Eq. 9 represents an over-determined least-squares system of equations, it is amenable to later direct inversion using simple matrix algebra. We assume there are *J* time samples total, running over the subscript *j*; there can be time gaps (much as there often are in tidal analyses), but the total number of samples should be equal to or greater than the number of unknown temporal coefficients, *N*; thus, the problem will be over-determined. The goal is to calculate the unknown temporal modal coefficients $B_n^{(i)}$ from the *J* time samples of OMA coefficients $A_j^{(i)}$ based on immediately past data and then use these to forecast into the future. The solution for $B_n^{(i)}$ above is done using a linear least-squares fitting.

The method described above in Eq. 9 resembles in some of the terms the well-known and accepted T_TIDE methodology for tidal analysis used by oceanographers (Pawlowicz et al. 2002). So a question: Why not use T_TIDE to extract tidal constituents? Firstly, there are other terms that are important on a short-time basis not included in T_TIDE capability (constant, linear trend, inertial oscillations). Secondly, over a short time history of 12 h, it is impossible to resolve the 37 individual tidal constituents in T_TIDE that is normally applied to months of time series data. For example, one cannot possibly resolve the closely spaced M2 from the S2 (semidiurnal) nor the K1 from the O1 (diurnal) frequencies. Therefore, a single semidiurnal and diurnal is adequate. Asking for too much poorly resolved modal data (as with OMA discussed earlier) will lead to instabilities in the fitted coefficients, making things worse than better.

For the model hypothesized above with N=8 modal coefficients, the elements of the rectangular model matrix can be represented as follows:

$$\left[M_{j,n}\right] \equiv \begin{bmatrix} 1 & t_1 & \cos(f_1 t_1) & \sin(f_1 t_1) & \cos(f_2 t_1) & \sin(f_2 t_1) & \cos(f_o t_1) & \sin(f_o t_1) \\ 1 & t_2 & \cos(f_1 t_2) & \sin(f_1 t_2) & \cos(f_2 t_2) & \sin(f_2 t_2) & \cos(f_o t_2) & \sin(f_o t_2) \\ \cdots & \cdots & \cdots & \cdots & \cdots & \cdots & \cdots & \cdots \\ 1 & t_j & \cos\left(f_1 t_j\right) & \sin\left(f_1 t_j\right) & \cos\left(f_2 t_j\right) & \sin\left(f_2 t_j\right) & \cos\left(f_o t_j\right) & \sin\left(f_o t_j\right) \\ \cdots & \cdots & \cdots & \cdots & \cdots & \cdots & \cdots & \cdots \\ 1 & t_J & \cos(f_1 t_J) & \sin(f_1 t_J) & \cos(f_2 t_J) & \sin(f_2 t_J) & \cos(f_o t_J) & \sin(f_o t_J) \end{bmatrix} \tag{10}$$

We may find that not all of the eight modal terms are needed or are in fact helpful for short time series. In fact, this is the case for our study here, which is examined subsequently. If not all of the modal terms are needed,

columns of the model matrix 10 above should be omitted.

(c) Solving for the STPS modal temporal coefficients: With the model matrix represented in Eq. 10 above determined at each of the time points from the known OMA coefficients $A_j^{(i)}$, the over-determined system of equations is solved using any standard approach. We choose MATLAB where the solution is denoted by the backslash operator as follows:

$$\left[B_n^{(i)}\right] = \left[M_{j,n}\right] \backslash \left[A_j^{(i)}\right] \tag{11}$$

(d) Forecasting ahead a few hours: Except for rapidly changing winds and their effects on the surface currents, the coefficients for the N temporal modes, $B_n^{(i)}$, that we have determined above will allow us to forecast ahead, perhaps for as long as the database period used to calculate the coefficients. Let us assume we want to forecast ahead starting at our last time observation, t_J, going up through t_{J+k}. One does this by constructing the new model matrix for times up through time k and performing a forward matrix multiply:

$$\left[A_{J+k}^{(i)}\right] = \left[M_{J+k,n}\right]\left[B_n^{(i)}\right] \tag{12}$$

Then, from these new "forecasted" OMA coefficients as a function of time, one creates the total vector fields at these future times t_{J+k}. From these consecutive OMA-forecasted current fields, one can determine mathematical surface trajectories starting at present time t_J up through any future time t_{J+k}.

4 Performance of the STPS methodology

In order to test the above STPS methodology, we use the data for the period from September 14, 2010, 21:00 UTC through September 30, 2010, 22:00 UTC gathered during the NOFO rapid-response field trial (NOFO final report). This overall period is divided in 16 24-h sub-periods (12 h of fitting analysis and 12 h of forecast), for which we perform statistical accuracy estimates of the "forecast skill" presented in the subsequent sections.

4.1 Forecast skill applied to OMA mode coefficients

A measure of forecast accuracy or skill is the departure of the OMA coefficients over time from the forecasted coefficients. We present this analysis here for the 16 24-h NOFO data periods. These are summarized in the subsequent tables for the three sets of OMA modes, where each set of OMA mode statistics has been averaged over the 12-h forecast period. Here, 15 Neumann modes, 7 Dirichlet modes, and 12 boundary modes were selected, as discussed earlier (not necessarily an optimum mode-set selection). The first column defines the mode number as represented by the index of its eigenvalue. The OMA coefficient, A, is directly proportional to velocity, and therefore, the square of the coefficient, A^2, is directly proportional to the kinetic energy in each mode given that all other constants and factors are the same for all modes. This provides a convenient method for evaluating the portion of total kinetic energy present in each mode without carrying unnecessary factors or units. The rows and modes have been sorted in importance according to this relative kinetic energy, labeled "A^2 Energy," that has been averaged over 12 forecast hours and 16 such periods; this is found in the second column. Then the mean square difference of OMA coefficients (forecasted vs. actual) is given in the third column. Finally, the mean square difference ratio is listed as the fourth column (i.e., it is the quotient of the third column divided by the second). The latter perhaps is more meaningful because it is based on the energy in that mode; sometimes this is referred to as the coefficient of variation (Tables 1, 2, and 3).

Energy in modes as a criterion for how many are important
With a vast number of possible modes, one must make a choice of how many to include in the analysis to reproduce the current field. There is not a cost of computing power, but including too many modes makes the higher ones much more sensitive to small spatial scale noise or gaps. This in turn begins to affect the accuracy of the lower-order mode

Table 1 Energy and forecasted OMA coefficient difference variances in the 15 Neumann modes, averaged over 16 24-h time periods

Mode number	A^2 energy	Mean square difference	Mean square difference ratio
2	60.3999	14.4505	0.2392
1	19.5738	0.7129	0.0364
3	14.2121	1.7104	0.1203
15	11.2430	5.3935	0.4797
9	10.4539	5.4348	0.5199
10	9.5369	5.2894	0.5546
6	9.0137	5.3626	0.5949
4	8.5229	1.7724	0.2080
8	7.8340	3.5327	0.4509
7	7.0914	3.4014	0.4797
11	6.4449	3.7293	0.5786
5	5.6445	6.6702	1.1817
12	5.5679	2.7968	0.5023
14	5.0982	2.8441	0.5579
13	3.7792	2.2429	0.5935

Table 2 Energy and forecasted OMA coefficient difference variances in the seven Dirichlet modes, averaged over 16 24-h time periods

Mode number	A^2 energy	Mean square difference	Mean square difference ratio
1	56.4645	1.8979	0.0336
2	21.0345	6.0414	0.2872
4	20.6288	3.7860	0.1835
5	4.7870	2.4480	0.5114
7	4.0265	3.7171	0.9232
6	3.0259	1.4542	0.4806
3	2.5634	0.9501	0.3706

coefficients when attempting to extract too many (Lekien and Gildor 2009). As one follows down the second columns of the above tables, one gains an appreciation for the cumulative total energy to that point and estimate how much might be lost by dropping everything below that row from consideration. Before settling on the somewhat arbitrary selection of 34 modes done earlier, we decided to examine a truncated number of modes based on cumulative energy, i.e., selecting the most energetic. We tried the following, leading to 13 total instead of 34.

Neumann modes: Cut off below the sixth row, so that modes [2, 1, 3, 15, 9, 10] are included. This set contains nearly 70% of the total energy (i.e., sum of first six divided by sum of total).

Dirichlet modes: Cut off below the second row, so that modes [1, 2] are included. As in the case of the Neumann modes, this set contains about 70% of the total energy.

Boundary modes: Here we cut off everything below the fifth row, including modes [7, 3, 2, 9, 8]. This set contains about 75% of the total energy.

Table 3 Energy and forecasted OMA coefficient difference variances in the 12 boundary modes, averaged over 16 24-h time periods

Mode number	A^2 energy	Mean square difference	Mean square difference ratio
7	17.5808	0.8093	0.0460
3	15.2467	5.0625	0.3320
2	15.0909	4.1015	0.2718
9	11.9052	1.6728	0.1405
8	11.7794	1.1856	0.1007
4	6.1820	3.0168	0.4880
10	4.0599	1.4688	0.3618
12	3.7742	0.6723	0.1781
5	3.3561	1.5423	0.4596
11	2.7091	2.1722	0.8018
6	2.4491	1.0804	0.4412
1	1.6209	0.9934	0.6128

As a quality measure and basis for a decision whether this reduced mode set is a better choice, we compared the OMA mode fit to total currents with the conventional LS total currents over all 16 NOFO time periods of 24 h each, exactly as we did to calculate and plot Fig. 4. This is shown below as Fig. 5.

The overall RMS difference summaries for these Fig. 5 plots are 11.0 and 9.7 cm/s for U and V, respectively. This compares to 8.0 and 7.6 cm/s when all 34 modes were used for the Fig. 4 comparisons. Although the differences are not large, they are significant. Therefore, we stayed with our original selection of 34 modes for all subsequent analyses and comparisons.

4.2 Surface current forecast skill

In this section, we show a statistical analysis of the differences between the forecasted currents obtained from the above STPS versus the actual (nowcast) OMA fits to HF radial current observations. The later are considered as the benchmark for quantifying the skill of the forecast. Keep in mind that, for statistical consistency, we perform that analysis for all the 16 24-h selected periods, but we show here examples for certain periods. As explained in Section 3, the first 12 h for each set is the analysis period where the OMA coefficients are fitted, and the subsequent 12 h is the forecast period.

In Fig. 6, we present the temporal evolution of the mapped-average RMS difference between the OMA nowcast current field and the STPS currents for the 16 24-h periods used in the study. This comparison is performed for both U and V components, separately. Note that the RMSE stays low during the first 12 h since this is the analysis period where the OMA temporal mode coefficients are fitted to the observed hourly OMA coefficients. Following the transition to the forecast period, the RMS error tends to increase over the next 12 h as expected.

There are three periods that stand out as worse than others: #3 (green), #15 (blue), and #16 (red). We examine period #3 later, as a case of a wind reversal that is not accounted for in the present STPS methodology. Otherwise, forecast RMS errors are less than 10 cm/s, which is reasonable in light of overall NOFO current magnitudes and results that would be incorrectly predicted by persistence.

As all time periods have similar behaviors, we focus here in one particular example from 15th September 13:00 to 16th September 12:00 (period #2). We can see in Fig. 7 how the forecasted currents fields are very similar, after 12 h of prediction, to the OMA nowcast currents.

4.3 Comparison with persistence

In meteorology and occasionally in oceanography, "persistence" is suggested for short-term forecasts. This simply consists of continuing the latest nowcast condition into the future, as a constant term. Because of its popularity, we

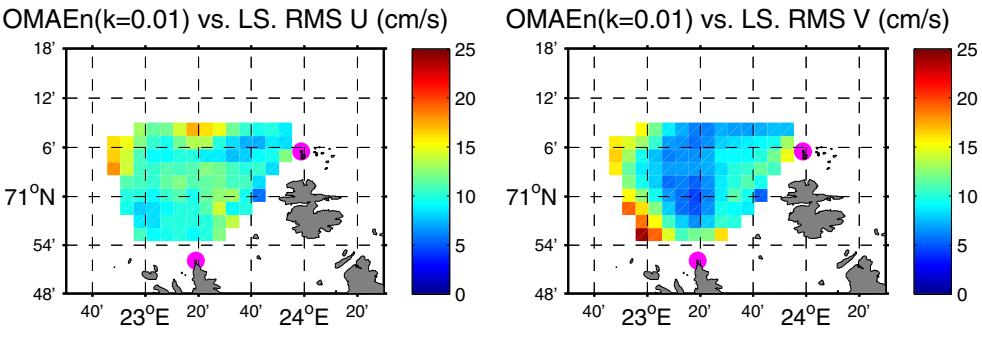

Fig. 5 Root mean square (*RMS*) of the differences between the OMA-radial-fitted vector fields and the LS method for all of the aforementioned 16 24-h periods for the reduced mode set of 13 rather than 34 modes used in Fig. 4

show below in Fig. 8 the error results based on persistence (red curve) for the period #2 example we have been examining above. This is compared with currents from our nowcasted (first 12 h) and STPS-forecasted (second 12 h) currents (blue curve). Both represent the RMSE between the actual OMA coefficients for each hour and the respective time model for period #2: OMA+STPS (blue) vs. persistence (red). For the first 12 h, persistence error is zero because this is the actual current before persistence of the last point projects it into the future. As one advances into the second 12-h half, representing the forecast period, RMSE for persistence becomes very large as expected because it misses the tidal variation. It drops at the end of the period after 12 h because the semidiurnal tidal cycle returns to nearly its value at the beginning.

The error in using persistence for the other 15 time periods is always larger than the STPS forecast errors, as expected. For some cases, it is much worse than it is in Fig. 8 while for other cases better. Therefore, persistence cannot be recommended over periods extending more than a couple hours at most into the future for ocean current forecasting.

4.4 Trajectory forecast skill

As another measure of forecast skill for the STPS technique, we computed the trajectories followed by multiple virtual particles released in the NOFO domain area and being transported by the ocean currents derived from the HF observations. We then compared the trajectories of the virtual particles forced by the OMA nowcast currents and by the STPS-derived currents. Thirty-three particles were released, one each third grid point (9 km). We show in Fig. 9 the simulated trajectories for period #2, whose current predictions we examined above (14th September 21:00 to 15th September 20:00). We observe good behavior for the short-term forecast trajectories, in that the nowcasted (black) and forecasted (blue) curves visibly nearly overlay each other after starting at the same initial point (red dot).

For the sake of comparison, we present also in Fig. 10 the trajectories for period #3, where a wind event caused a large RMSE of the currents, the worst scenario in Fig. 6 (green). One sees that although the forecasted (black) and nowcasted

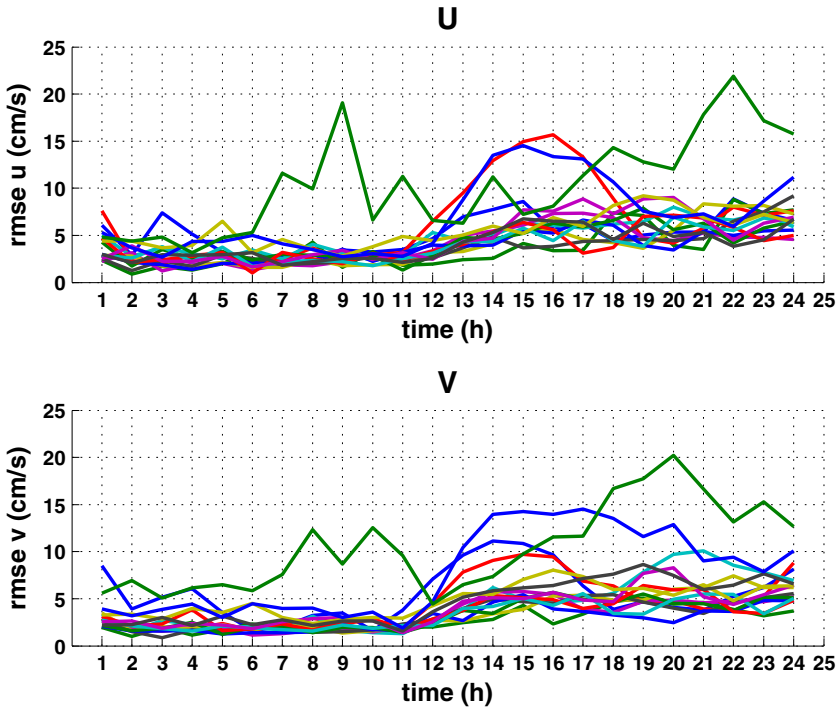

Fig. 6 Spatially averaged RMS of the difference between the nowcast OMA current fields and the STP fields for the 16 periods and for *U* and *V* components separately. Each *color* represents one 24-h period used in this study

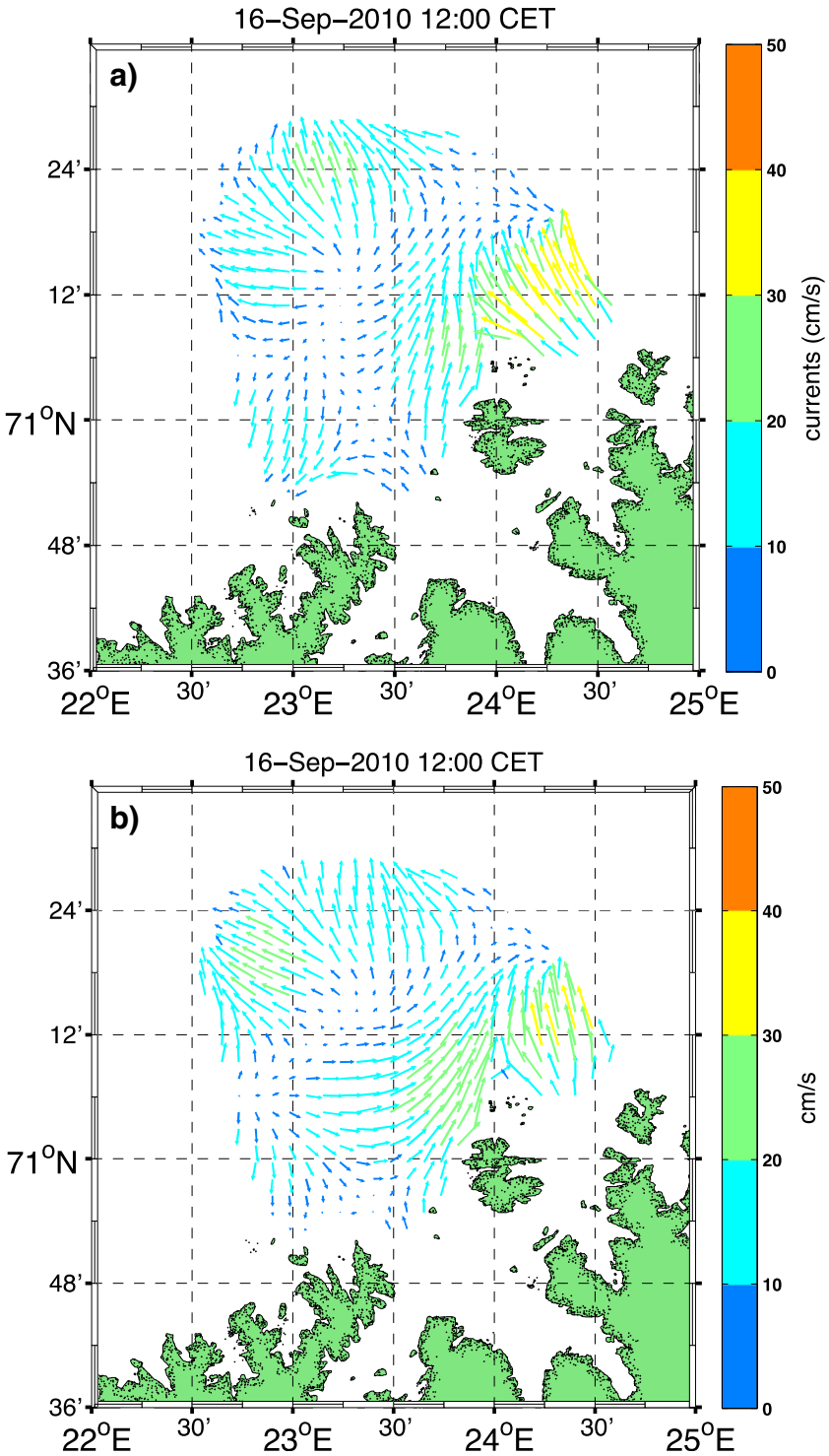

Fig. 7 OMA surface velocity field for the NOFO area for period #2 (15th September 13:00 to 16th September 12:00). **a** Predicted field at the end of the 12-h forecast; **b** OMA-fitted currents nowcast surface current field at the same time

OMA trajectories follow the same general paths, they depart from each other to a greater extent toward the end of their trajectories.

To quantify the forecast skill shown in the trajectory maps, we calculated the average distance divergence between trajectories from actual vs. forecasted OMAs for all particle trajectories represented in Fig. 9 (corresponding to period #2). As expected, the distance divergence increases with time in the forecasted period (after 12 h of initial analysis). However, the distance divergence is less than 1.5 km (Fig. 11), which is considered good agreement for a 12-h forecast. Compare this to the trajectory divergences for the worst period that was influenced by a wind change, period #3, in Fig. 12, where final separation distances cluster around 3–4 km.

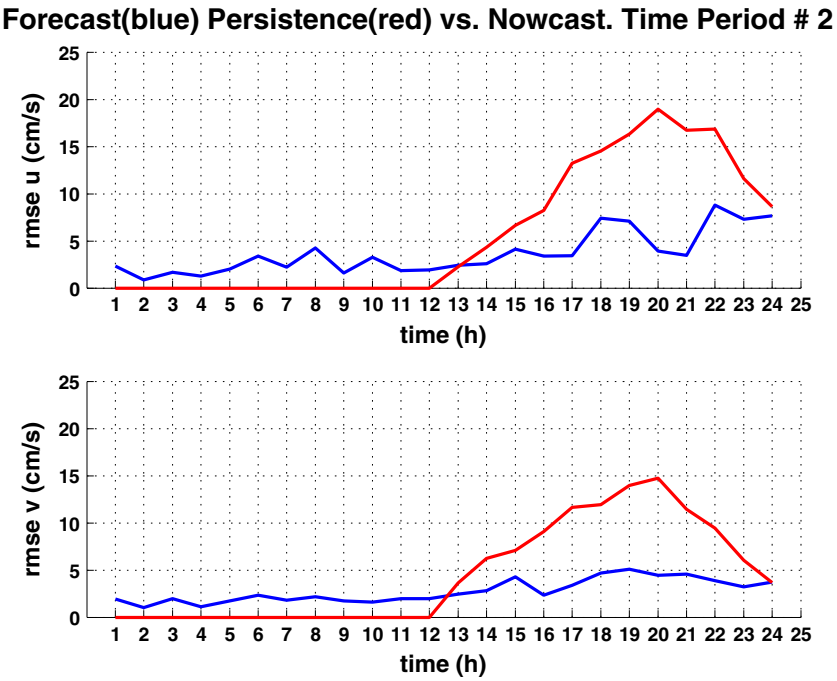

Fig. 8 Comparison of RMS current vector errors over area for period #2 (14th September 21:00 to 15th September 20:00). This compares simple persistence error (*red*) with nowcasted (first 12 h) and STPS-forecasted (second 12 h) time history (*blue*)

5 A case study of wind influences

The STPS methodology that we presented in Section 3 and tested against NOFO data assumed a temporal model over 12-h periods that included effects that are predicable from the immediate past: tides, inertial harmonics, constant, linear trend. Wind also influences surface currents seen by the radars. A changing wind, however, is not predictable from past surface current behavior. Future work must augment the present STPS based on estimates of wind forecasts in the local area of radar measurement. This should improve the current forecasts.

We highlight here period #3 (16th September 09:00 to 17th September 08:00, 2010) as an example suggesting that a changing wind was responsible for the worst forecast agreement of the 16 periods we examined. From the hindcast

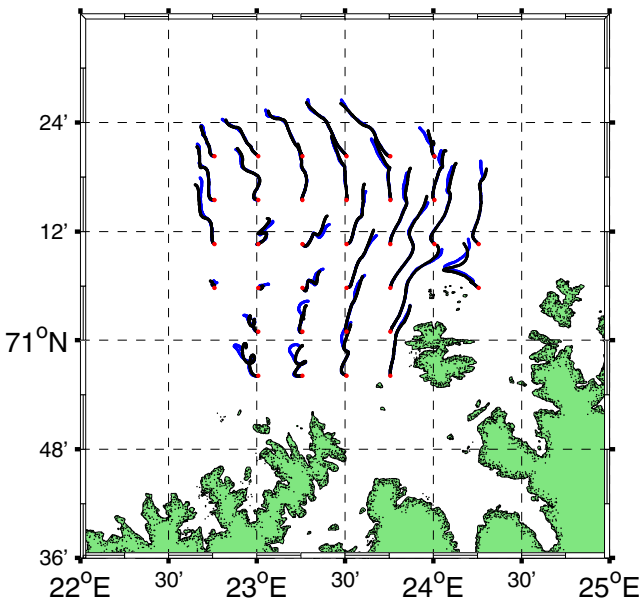

Fig. 9 Simulated trajectories followed by virtual particles (initial positions are the *red points*) being forced by actual OMA-fitted currents (*blue lines*) and by forecasted OMA currents (*black lines*). The trajectories are from period #2 from 14th September 21:00 to 15th September 20:00, 2010

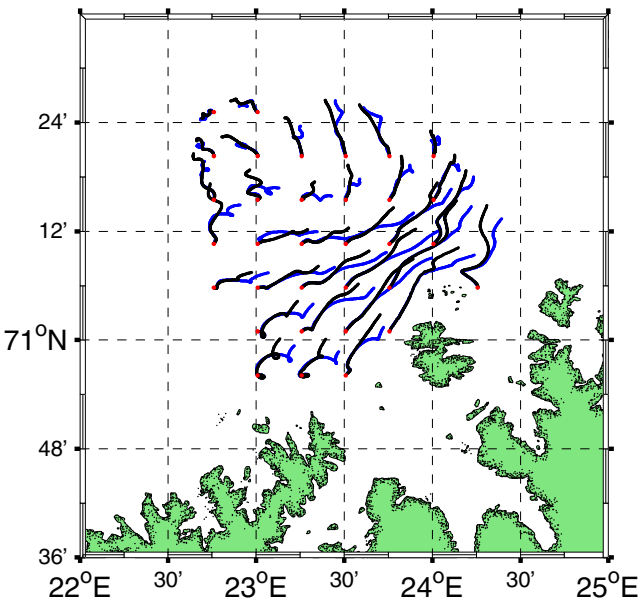

Fig. 10 Simulated trajectories followed by virtual particles (initial positions are the *red points*) being forced by actual OMA-fitted currents (*blue lines*) and forecasted OMA currents (*black lines*). The trajectories are from period #3 from 16th September 09:00 to 17th September 08:00, 2010

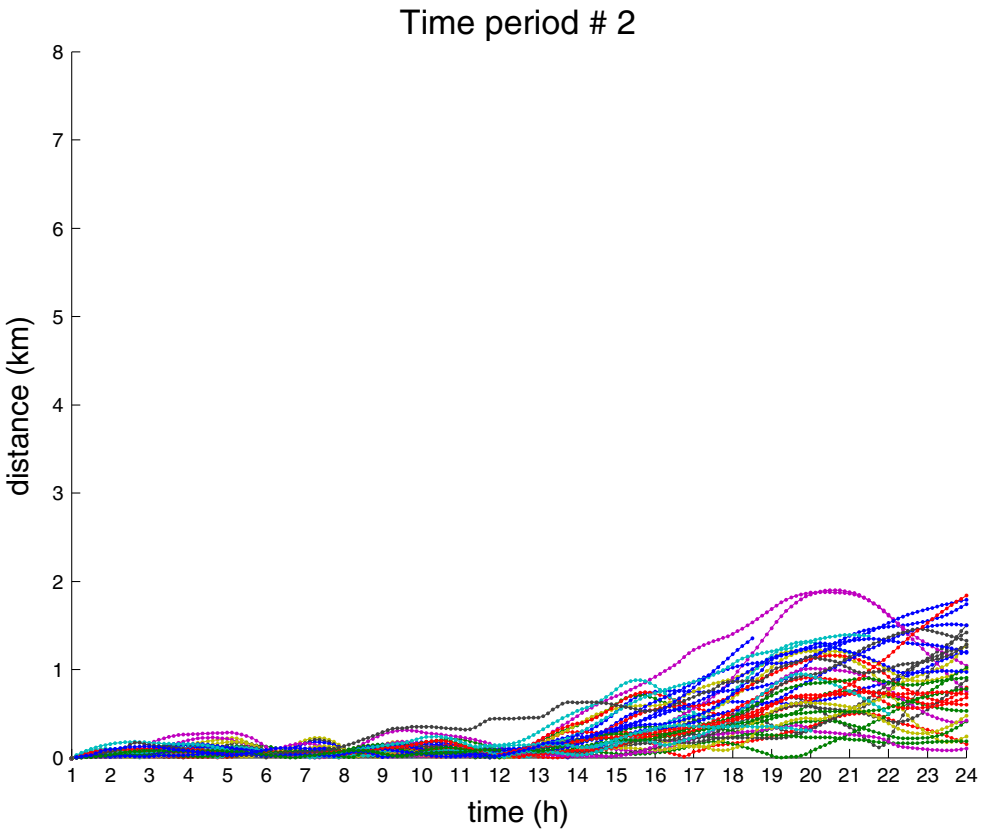

Fig. 11 Temporal evolution of distance divergences between trajectories with actual OMA currents vs. forecasted OMA for period #2. Each *color* follows a virtual particle in Fig. 9

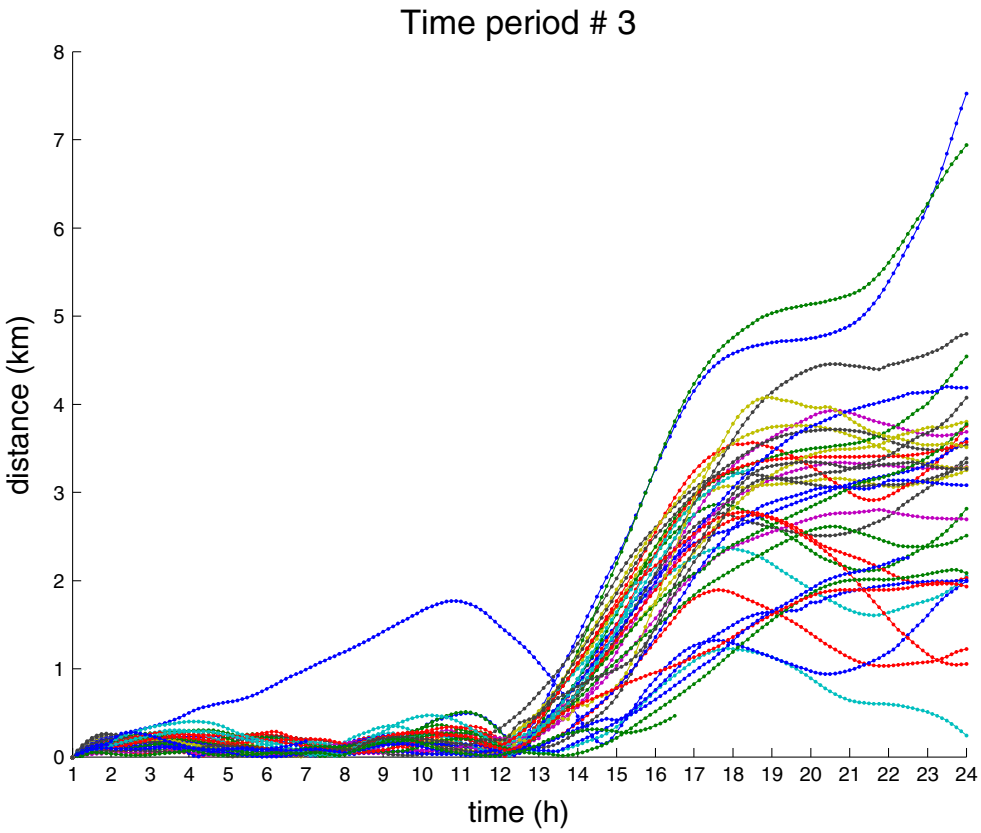

Fig. 12 Temporal evolution of distance divergences between trajectories with actual OMA currents vs. forecasted OMA for period #3. Each *color* follows a virtual particle in Fig. 10

archive NORA10 provided by the Norwegian Meteorological Institute (Reistad et al. 2011), we have an estimate of the wind behavior over the radar area. The general direction and speed of the wind over this region during September was typically in the range of 4–8 m/s from a northwesterly direction. However, a frontal passage or storm system caused a wind reversal to a direction from the east during the period between the 15th and early 16th of September, with speed increasing to 10–11 m/s.

During the NOFO period, the most energetic OMA modes that best fitted the radial surface current data were: Neumann mode #2, Dirichlet mode #1, and boundary mode #7. Refer to Fig. 3 (left columns) to observe the current patterns represented by these three energy-dominant modes. The normal temporal behavior of the dominant OMA coefficients reflects the semidiurnal tidal nature of the flows, plus a constant (persistence) term over these 24-h periods under consideration. However, Neumann Mode #2 saw an anomaly during the beginning of this period. We illustrate this by showing the modal coefficient history during this period #3 in Fig. 13. The green and black curves are the dominant Dirichlet and boundary modal coefficients, respectively. They clearly exhibit the constant and semidiurnal behavior expected of tides. The red curve is the Neumann dominant mode coefficient, which is missing the first tidal period that would have shown a downward dip.

How is this behavior explained in terms of the wind change? The wind direction during this initial part of the 24-h period had reversed so that it came from the east (with increased strength to ~11 m/s). This would have driven a current flowing to the northwest, following the expected Ekman rotation to the right. But this is precisely the positive direction of the dominant Neumann mode shown in the upper right of Fig. 3. This explains the canceling of the negative cycle of the red curve of Fig. 13 above that would have followed the tide. The wind-induced current flowing NW would not have affected either the dominant Dirichlet or the boundary modes shown in the left columns of Fig. 3 because their current directions have no significant overall orientations in this direction. Thus, their tidal nature is unperturbed by the wind-induced drift.

So now, our STPS formulation that models only tides and constant behavior tries to fit the semidiurnal harmonics and constant to the red curve of Fig. 13 over the first 12 h, in order to forecast it into the second 12-h period. Clearly the strong tidal behavior will be missing and contribute to an erroneous forecast for the second half of the 24-h period. To demonstrate and confirm these forecasted behaviors, we show in Fig. 14 the actual and the forecasted OMA coefficient behaviors. Green is the time forecast for the three dominant modes, while red is the actual. In the leftmost Neumann mode #2, one sees that the green forecasted behavior has little variation, based on the fact that the wind had canceled nearly all of the tidal variation during the first 12 h used to create the forecast; the red actual behavior had a strong negative tidal swing because the wind had relaxed, and the error between these two is very significant. On the other hand, the other two dominant modes (Dirichlet and boundary) that are not oriented so that they responded to this Easterly wind therefore did not have their forecasted behavior influenced negatively by the wind; their actual (red) and forecasted (green) behaviors follow each other nicely. Because this dominant Neumann mode had such high tidal energy during the forecasted period that was missed in our STPS prediction itself, this was sufficient to cause the departure of the forecasted current patterns and trajectories

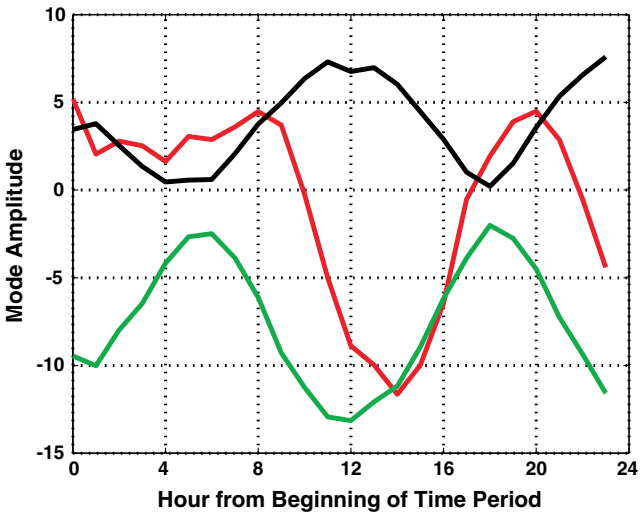

Fig. 13 Dominant OMA modal coefficients vs. time, fitted to radar data for the anomalous period #3 (16th September 09:00 to 17th September 08:00, 2010). *Red* is Neumann mode #2; *green* is Dirichlet mode #1; *black* is boundary mode #7

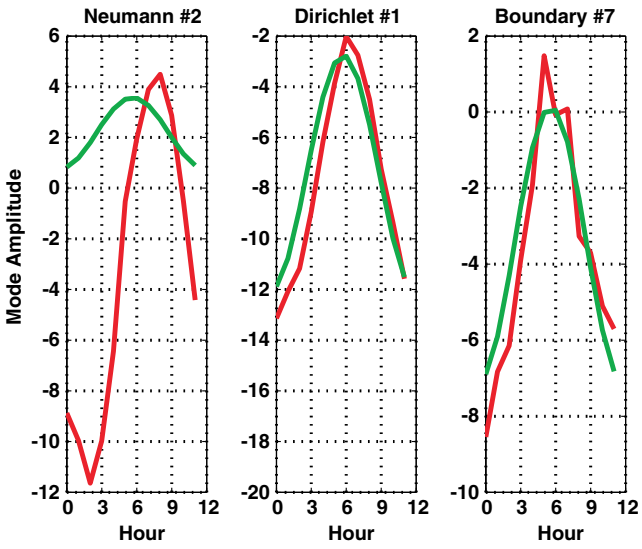

Fig. 14 Actual and forecasted dominant OMA mode coefficient time behavior during the prediction period of our STPS model. *Red* is the actual OMA-fitted coefficient history, while *green* is the forecasted based on the prior 12-h period. The Neumann mode completely misses the strong negative tidal cycle because of the prior wind influence

that were observed in earlier sections from the good prediction that one would have hoped for.

The rationale explained above also suggests a mode-based approach for including surface wind stress forecasts into our STPS model that will be implemented in future work. This is discussed further below.

6 Discussion

HF radar surface current nowcasts have been widely demonstrated to be very useful in practical oceanographic applications (e.g., Abascal et al. 2009). However, a STPS of surface currents based on HF radar data will be an even more useful extension for many practical applications, from SAR to oil spill operations. In this paper, we have introduced a simple, novel STPS methodology based on the prediction of the coefficients of OMA modes obtained after fitting the radial currents to a prior short set of hourly OMA coefficients (Kaplan and Lekien 2007; Lekien and Gildor 2009).

The methodology has been tested using the time history of HF data gathered in a rapid-deployment experiment in Finnmark (northern coast of Norway), during the execution of a NOFO funded project. For 16 sub-periods selected, a detailed statistical analysis of the RMS differences between the actual data (nowcast) and the forecasted data is presented for: (1) OMA representations of the mode coefficients, (2) the surface currents themselves before and after OMA fitting, as well as (3) for the surface trajectories determined from the OMA currents. Results show a good agreement between the forecasted and the actual fields. Three periods exhibit worse agreement; for the worst case, we discussed and showed that a wind reversal was responsible, which is not accounted for in our present STPS methodology.

We examined a number of tradeoffs in our OMA+STPS approach that have not been fully resolved within this short study and need further investigation. There are questions of: (1) an optimum setting for the homogenization smoothing parameter, k, that constrains the least-squares cost function so as to suppress spurious, large OMA coefficient velocities and (2) the choice of number of modes to be used and how the mode energy may play a role in this optimization. In our studies here, we have arrived at a selection for both, based on the fit of OMA total velocities to the conventional LS total velocities, using the minimization of RMSE between the two as a criterion. However, for both questions above, we find that STPS-forecasted currents—and especially trajectories—departed more from the OMA actual fits during the forecasted period when we optimized OMA parameters based on RMSE between actual LS and OMA-fitted totals. One can ask the question: Which is better, parameters that produce better OMA fits to the totals or parameters that give better forecasts because these two outcomes are somewhat different? Because we are determining the forecasts and their quality based on the OMA fits themselves, this leads to a somewhat circular argument. It will be resolved by further investigations involving validation exercises in which surface drifters are deployed and tracked for trajectory comparisons with OMA nowcast and forecast trajectories.

A second important future extension involves the few situations where changing wind over the analysis period (e.g., 24 h in our case) calls into question the simple temporal model based on past current history that we used here and will lead to the inclusion of wind forecasts. How might this be done? Our case study for period #3 here suggests the methodology we intend to develop. It will employ the OMA modes as described above for currents as its basis, leading to a straightforward blending of wind effects into our existing OMA+STPS methodology, with a set of forecasted OMA modes that will add in a special wind-produced set in the following way.

Wind imparts surface current momentum via the wind stress tensor, which is proportional to the square of the wind speed and has the direction of the wind vector. The dominant OMA modes (six of which are shown in Fig. 3) have distinctive vector patterns that will be more or less effective in coupling current flow to wind stress, depending on the wind direction over the radar-observed OMA domain and the mode pattern. Assuming to the lowest order that the wind field is uniform over these radar time and space scales, a table can be produced of the coupling between the wind from a given direction and a given OMA mode as the "dot-product" of the wind direction unit vector and each OMA mode pattern, over a direction grid of, say, every 15°. The expected Ekman rotation will be included in the wind-to-current directions. This results in a coupling or correlation matrix database, for which some modes are strongly coupled for given directions and others minimally. The strength of this coupling is related to assumed wind stress magnitude values, and we expect it will be directly proportional to the values of kinetic energy within the given mode, obtained as the squares of the vectors shown for each mode (as exemplified in Fig. 3), through a proportionality constant to be determined.

Tuning the above physics-based analytical foundation will be undertaken with measurements of winds over selected areas and supported by drifter measurements of the contemporary currents. We presently plan to study this for 5-MHz SeaSonde systems installed in Galicia, Spain and 13 MHz systems intended for future NOFO follow-up operations in Norway.

Acknowledgments The data used in this investigation were collected during the 2010 Rapidly Deployable HF Radar demonstration in Finnmark, Norway by the Norwegian company CodarNor AS with funding from the Norwegian Clean Seas Association for Operating Companies (NOFO) and Innovation Norway through an industrial

research and development contract. The Norwegian field work also received funding from the Oilwave project funded by ENI and the Research Council of Norway (NFR) through the PETROMAKS programme (grant no 207541) and from the Biowave project funded through the NFR programme "Havet og kysten" (grant no. 196438). V. Fernández and M.I. Ferrer hold the Torres Quevedo Grant no's. PTQ06-02-0930 and PTQ09-02-01454, awarded by the Spanish Ministry of Science and Innovation, by the European Regional Development Fund, and by the European Social Fund. The authors would like to personally thank Dr. Anton Kjelaas of CodarNor, Andres Alonso Martirena and Pedro Agostinho of Qualitas REMOS, Peter Lilleboe of CODAR Ocean Sensors, and Jørn Johansen of Polarbase AS for their invaluable contributions to this article and the success of the NOFO field trial.

References

Abascal AJ, Castanedo S, Medina R, Losada IJ, Alvarez-Fanjul E (2009) Application of HF radar currents to oil spill modeling. Mar Pollut Bull 58:238–248

Barrick DE, Evans MW, Weber BL (1977) Ocean surface currents mapped by radar. Science 198:138–144

Barrick DE (1979) A coastal radar system for tsunami warning. Remote Sensing Environ 8:353–358

Breivik Ø, Sætra Ø (2001) Real-time assimilation of HF radar currents into a coastal ocean model. J Mar Syst 28:161–182

Frolov S, Paduan J, Cook M, Bellingham J (2011) Improved statistical prediction of surface currents based on historic HF-Radar observations. Ocean Dynamics—Special Issue: SAR2011

Kaplan DM, Lekien F (2007) Spatial interpolation and filtering of surface current data based on open-boundary modal analysis. J Geophys Res 112(C12007), 20 pp

Kjelaas A, Whelan C, Lilleboe P, Fernandez Lopez V, Breivik Ø (2011) Rapid deployable HF Radar for oil spill response. Final report, Norwegian Clean Seas Association (NOFO) Oil Spill Response 2010 Technology Development Program

Lekien F, Coulliette C (2004) Open-boundary modal analysis: Interpretation, extrapolation, and filtering. J Geophys Res 109(C12004), 13 pp

Lekien F, Gildor H (2009) Computation and approximation of length scales of harmonic modes with application to the mapping of surface currents in the Gulf of Eilat. J Geophys Res 114(C06024), 24 pp

Lipphardt BL Jr, Kirwan AD Jr, Grosch CE, Lewis JK, Paduan JD (2000) Blending HF radar and model velocities in Monterey Bay through normal mode analysis. J Geophys Res 105(C2):3425–3450

Lipa BJ, Barrick DE (1983) Least-squares methods for the extraction of surface currents from CODAR crossed-loop data: application at ARSLOE. IEEE J Oceanic Engr OE8:226–253

Lipa BJ, Barrick DE (1986) Extraction of sea state from HF radar sea echo: mathematical theory and modeling. Radio Science 21:81–100

Lipa B, Barrick D, Saitoh SI, Ishikawa Y, Awaji T, Largier J, Garfield N (2011) Japan Tsunami Current Flows Observed by HF Radars on Two Continents. Remote Sensing 3:1–17

O'Donnell JD, Ullman MS, Howlett E, Fake T, Hall P, Tatsu I, Edwards C, Anderson E, McClay T, Kohut J, Allen A, Lester S, Lewandowski M (2005) Integration of Coastal Ocean Dynamics Applications Radar (CODAR) and Short-Term Prediction System (STPS) surface current estimates into the Search and Rescue Optimal Planning System (SAROPS). U.S. Coast Guard Tech. Rep., DTCG39-00-D- R00008/HSCG32-04-J-100052

Oke PR, Allen JS, Miller RN, Egbert GD, Kosro PM (2002) Assimilation of surface velocity data into a primitive equation coastal ocean model. J Geophys Res 107(C9):3122. doi:10.1029/2000JC000511

Paduan J, Shulman I (2004) HF radar data assimilation in the Monterey Bay area. J Geophys Res 109(CO7S09). doi:10.1029/2003JC001949

Pawlowicz R, Beardsley B, Lentz S (2002) Classical tidal harmonic analysis including error estimates in MATLAB using T_TIDE. Comput Geosci 28:929–937

Reistad M, Breivik Ø, Haakenstad H, Aarnes OJ, Furevik BR, Bidlot J (2011) A high-resolution hindcast of wind and waves for the North Sea, the Norwegian Sea, and the Barents Sea. J Geophys Res 116:C05019. doi:10.1029/2010JC006402

Roarty HJ, Lemus ER, Handel E, Barrick DE, Isaacson J (2011) Performance evaluation of SeaSonde high-frequency radar for vessel detection. Marine Tech Soc J 45(3):14–24

Ullman DJ, O'Donnell CE, Fake T, Morschauser D, Sprague M, Allen A, Krenzien LCDR B (2003) Use of Coastal Ocean Dynamics Applications Radar (CODAR) technology in U.S. Coast Guard search and rescue planning. Final report no. CG-D-09-03, U.S. Coast Guard Research and Development Center.

Ullman DS, O'Donnell J, Kohut J, Fake T, Allen A (2006) Trajectory prediction using HF radar surface currents: Monte Carlo simulations of prediction uncertainties. J Geophys Res 111:14, C12005

Zelenke BC (2005) An empirical statistical model relating winds and ocean surface currents: Implications for short-term current forecasts, M.Sc. thesis, Oregon State University, Corvallis, OR